Dry granular avalanche impact force on a rigid wall: Analytic shock solution versus discrete element simulations

Adel Albaba*
University of Grenoble Alpes, Irstea, UR ETGR, 2 rue de la Papeterie-BP 76, F-38402 St-Martin-d'Hères, France and Berne University of Applied Sciences, School of Agricultural, Forest and Food Science HAFL, Länggasse 85, CH-3052 Zollikofen, Switzerland

Stéphane Lambert and Thierry Faug†
University of Grenoble Alpes, Irstea, UR ETGR, 2 rue de la Papeterie-BP 76, F-38402 St-Martin-d'Hères, France

(Received 13 July 2017; revised manuscript received 12 March 2018; published 21 May 2018)

The present paper investigates the mean impact force exerted by a granular mass flowing down an incline and impacting a rigid wall of semi-infinite height. First, this granular flow-wall interaction problem is modeled by numerical simulations based on the discrete element method (DEM). These DEM simulations allow computing the depth-averaged quantities—thickness, velocity, and density—of the incoming flow and the resulting mean force on the rigid wall. Second, that problem is described by a simple analytic solution based on a depth-averaged approach for a traveling compressible shock wave, whose volume is assumed to shrink into a singular surface, and which coexists with a dead zone. It is shown that the dead-zone dynamics and the mean force on the wall computed from DEM can be reproduced reasonably well by the analytic solution proposed over a wide range of slope angle of the incline. These results are obtained by feeding the analytic solution with the thickness, the depth-averaged velocity, and the density averaged over a certain distance along the incline rather than flow quantities taken at a singular section before the jump, thus showing that the assumption of a shock wave volume shrinking into a singular surface is questionable. The finite length of the traveling wave upstream of the grains piling against the wall must be considered. The sensitivity of the model prediction to that sampling length remains complicated, however, which highlights the need of further investigation about the properties and the internal structure of the propagating granular wave.

DOI: 10.1103/PhysRevE.97.052903

I. INTRODUCTION

Granular materials are ubiquitous in many applications, including the transport of particles in industry and granular flows in geophysics. The problem of granular avalanche flows interacting with rigid obstacles down an incline has attracted great attention in recent years [1–11], and it still deserves investigation [12], because it is particularly relevant to mitigation against granular flows in nature, such as debris flows, rock avalanches, and snow avalanches. The huge damage those flows can cause to civil engineering structures (protection dams, buildings' walls, critical infrastructures) motivates research on the impact force of granular flows on a rigid wall.

The problem of the impact of a granular mass flowing down an incline and then impacting a rigid wall, with overflow being prevented downstream of the wall, has been investigated in the past using various approaches, including laboratory tests [2,4,10] and numerical simulations based on either depth-averaged equations [3] or the discrete element method [13]. When the flow meets the wall, it is pushed upstream of the wall, thus producing a sudden change in height and velocity, namely a hydrauliclike granular jump that propagates upstream from the wall. Some features of this granular jump traveling upstream of the wall, also called a granular bore [14], could be reasonably well captured by numerical simulations based on a depth-averaged model using shock capturing techniques [3,14].

The current paper proposes a simple analytic solution based on depth-averaged continuum approach, which accounts for the main physics of the problem: a compressible granular shock wave that travels upstream while a granular dead zone forms between the shock and the wall. The prediction of this analytical model for the impact force on the wall is carefully tested over a wide range of slope angles, against new numerical simulations using the discrete element method (DEM), earlier developed and validated on laboratory tests (see Ref. [15]). The cross-comparison between the analytic force model proposed and the DEM simulations allows us to put emphasis on some important aspects related to the role of fluid-solid coupling in granular matter and to the highly dissipative nature of granular materials.

The paper is organized as follows. Section II describes the DEM simulations. In Sec. III, the analytical force solution based on depth-averaged compressible shock wave theory is derived. Section IV addresses the comparison between the prediction of the analytic force model and the DEM simulations. Finally, an extended discussion is given on the

*adel.albaba@bfh.ch
†thierry.faug@irstea.fr

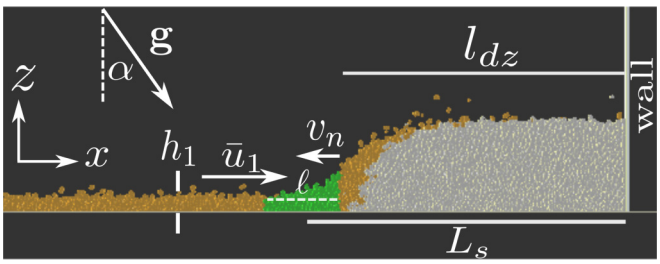

FIG. 1. Granular jump forming and propagating upstream of a wall of semi-infinite height, while grains are trapped between the jump and the wall: general view extracted from the DEM simulations (example for $\alpha = 30^\circ$). See text for notation. The region in brown corresponds to the undisturbed incoming flow. The regions in white (dead zone) and green (virtual box that roughly matches the jump length) will be defined in Secs. II B 3 and II B 2, respectively.

major outcomes of the present study and some challenging perspectives regarding the physics of the impact of granular flows with boundary rigid walls (Sec. V).

II. DISCRETE ELEMENT SIMULATIONS

A. Method, contact law, validation

The discrete element simulations conducted in the present study are based on molecular dynamics [16]. The contact laws between grains are a viscoelastic force for the normal contact and an elastic force for the tangential contact restricted to a Coulomb threshold. Details are given in Appendix A.

The DEM simulations are used here to model a granular avalanche that propagates down an incline of slope α and constant width w under gravity acceleration g and then impacts a rigid wall. Note that the DEM model has been previously calibrated and validated [15,17] on some specific laboratory tests on granular flow impact on rigid walls [10], as detailed in Appendix B.

The granular avalanche before impacting the wall is defined by the following quantities: its thickness h_1, its depth-averaged velocity $\bar{u}_1 = \int_0^{h_1} u(z)dz$, and its mean volume fraction ϕ_1. The flow impacts a rigid wall of semi-infinite height, normal to the flow-bottom. As such, overflow downstream of the wall is prevented. This means that the whole incoming stream is forced to be pushed upstream from the wall. The interaction between the avalanche flow and the wall then produces a granular jump—a discontinuity in height and velocity—that propagates upstream, while grains are increasingly trapped between the jump and the wall. A general picture of this complicated physics, where both a propagating hydrauliclike jump and a solidlike dead zone coexist, is drawn in Fig. 1. The grains trapped between the wall and the rigid wall form a dead zone of length l_{dz} at the bottom (region in white in Fig. 1). The distance at which the jump propagates, with speed v_n, from the rigid wall is named L_s. The region in green in Fig. 1 roughly matches the jump volume before the dead zone. Its length ℓ corresponds to the x distance between the first point for which $z > h_1$ and the first point for which grains at the bottom are static (trapped inside the dead zone).

B. Geometry of the problem and measurements

1. Flow geometry

Granular samples were made of particles with uniformly distributed diameters ranging from 12.5 to 25 mm and thus having a mean diameter $d_{50} = 18.75$ mm. Each particle was then replaced with an equivalent volume of two overlapping particles (refer to Appendix B for details). These samples were prepared in a rectangular reservoir that was $140d_{50}$ long, $16d_{50}$ wide, and $20d_{50}$ high. Particles had an intrinsic particle density $\rho_P = 2700\,\mathrm{kg\,m^{-3}}$. Loose package of particles is generated at the beginning, where the total mass of each granular sample being 223.3 kg. Afterwards, under gravity deposition, particles get deposited at the bottom of the reservoir creating a dense and static sample. Once this step is achieved, the flow simulation starts by opening up the reservoir's gate instantly in a dam-break manner, thus allowing the particles to flow down the chute. The chute was $548d_{50}$ long, $16d_{50}$ wide, and $20d_{50}$ high. The chute was bound at its lower end by a semi-infinite rigid wall spanning the entire width of the chute, thus preventing overflowing downstream of the wall. Different DEM tests were carried out varying the inclination angle α of the chute. The interparticle friction φ was 40° and the microscopic friction angle of the chute bottom was 25°. Note that we considered a microscopic friction for the rigid wall (friction angle of 15° smaller than φ) and we implemented lateral walls with friction too (friction angle of 21° smaller than φ). Those specific values were initially motivated by previous calibration of the DEM model on existing laboratory tests (see Appendix B).

2. Incoming flow conditions (before the shock wave)

From the DEM simulations, the incoming flow was characterized at any position and any time by the following continuum quantities: its thickness h, its depth-averaged velocity $\bar{u}$, and its volume fraction ϕ. The dead zone was characterized at any time by its length l_{dz}, height h_{dz}, surface S_{dz}, and volume fraction ϕ_2 (we use here ϕ_2 in lieu of ϕ_{dz} in the spirit of the depth-averaged shock wave model described in Sec. III).

For the flowing part, a virtual box is used with a length equal to $15d_{50}$ at a distance l_{dz} away from the wall (see below in Sec. II B 3 how l_{dz} was calculated from DEM). This virtual box was designed to follow the shock interface as l_{dz} increases with time, in accordance with the assumptions made for the shock wave model derived in Sec. III. Within this box (see the green region shown on the snapshots in Figs. 1 and 4), the average thickness, depth-averaged flowing velocity, and mean volume fraction of the flow were derived, thus defining the features of the incoming flow: h_1, $\bar{u}_1$, and ϕ_1. Those data are the key input parameters that will be used to feed the analytic force model based on depth-averaged shock wave theory (Sec. IV). The length of that virtual box was chosen as $15d_{50}$ to be sufficiently large for averaging purpose, as a too small box would result in very disturbed flow properties that are too close to the shock wave surface. In contrast, a too large box would lead to having flowing properties very far away from the shock interface, in contradiction with the assumptions of the required inputs of the shock wave model presented in Sec. III. The influence of varying the sampling length on the model prediction will be presented in Sec. V A.

The thickness of the flow was calculated as follows: $h = 2\sum_{i=1}^{n} z_i/n$, where z_i is the distance between the flow-bottom and the mass center of each particle within the virtual sampling box, and n is the number of particles within this box. The average flowing velocity in the direction of the flow (along the slope) was calculated as follows: $u = \sum_{i=1}^{n} v_{xi}/n$, where v_{xi} is the flowing velocity in direction of the flow of each particle within the virtual sampling box. Then, the volume fraction was calculated as follows: $\phi = \sum_{i=1}^{n} m_i/(\rho_P 15 d_{50} wh)$, where m_i is the mass of a particle i within the sampling box.

3. *Dead zone and impact force*

To identify the dead zone (the white region upstream of the wall which is shown on the snapshots in Figs. 1 and 4), a criterion was adopted that defines a dead particle as the one that has a velocity v_x, in the main direction of the flow, lower than a threshold velocity. The latter was chosen to be $v_x < 0.05\max(u, 0.05u_{\max})$, following ideas in Ref. [18].

At each time step, after identifying the dead zone, its length (l_{dz}) was calculated as twice the average distance of all dead particles from the rigid wall, in the direction of the flow (in the spirit of the depth-averaged model described in Sec. III). The dead zone height against the wall (h_{dz}) was also calculated. It is worthwhile to note here that the method described above to extract the quantities l_{dz} and h_{dz} from DEM was not checked against another method but gave consistent results when compared to the snapshots as the ones shown in Figs. 1 and 4.

Next, to compute the mean volume fraction inside the dead zone, a virtual sampling box was assumed within the dead zone, at a distance equal to $l_{\mathrm{dz}}/2$ and $h_{\mathrm{dz}}/2$ horizontally and vertically away from the toe of the wall, respectively. The calculation within this box was similar to the one for ϕ_1. The side surface of the dead zone S_{dz} was then calculated as $M_{\mathrm{dz}}/(\rho_P \phi_{\mathrm{dz}} w)$, where M_{dz} is the mass of the dead zone.

Finally, the normal impact force F_n on the wall was calculated as follows: $F_n = \sum_{i=1}^{n} F_{ni}$, where F_{ni} is the normal force between a particle i and the wall, and n is the number of particles in contact with the wall.

C. Phenomenology of the impact with the wall

This section describes the main results from DEM simulations regarding the complicated phenomenology of the impact of the granular avalanche with the rigid wall. Different slope angles, ranging from 30° to 55°, have been investigated where the normal force applied on the wall has been recorded, in addition to the properties of the flowing part and the dead zone during the granular flow-wall interaction.

1. *Normal force applied to the wall*

The evolution of the normal force applied to the wall recorded with time for a range of the chute's inclination angles α is displayed in Fig. 2. The maximum and residual force values are found to be strongly influenced by α. For the highest α, a very high peak force is recorded within a short impact time. In addition, a high residual force is observed. For lower α, lower peaks and residual forces are recorded. Moreover, the ratio of peak to residual force (see inset in Fig. 2) decreases and drops to unity at $\alpha = 30°$ (no peak).

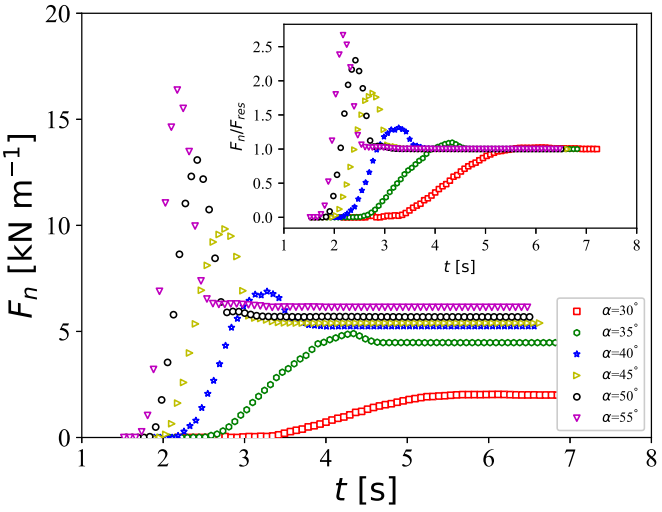

FIG. 2. DEM simulations. Evolution of the normal impact force F_n with time for different inclination angles α. Inset: the same data is shown in terms of F_n scaled by the residual force F_{res}.

This overall behavior could be linked to the kinetic energy of the flow, which increases with α due to the increase of the flowing velocity. This is consistent with a couple of previous studies: either granular flows interacting with rigid wall of semi-infinite height that prevented overflow [10,17] (as studied in the current paper) or granular flows passing over rigid walls small in size [19,20].

Checking the evolution of the dead zone may be an indicator of the static contribution to the total force. Figure 3 shows the relation between the normalized mass of the dead zone and the normal force normalized by the residual force, for different inclination angles. It can be seen that, for α as high as 55°, the peak force is reached while 30% of the dead zone

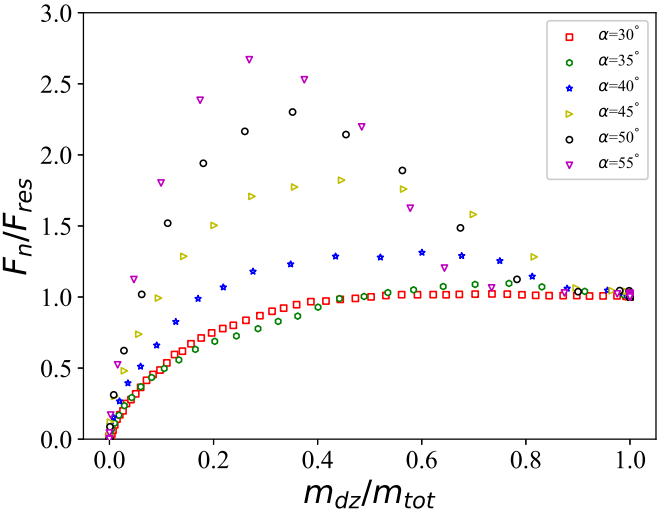

FIG. 3. DEM simulations. Evolution of the normal impact force scaled by the residual force, F_n/F_{res}, as a function of the dead zone mass normalized by the mass initially released, $m_{\mathrm{dz}}/m_{\mathrm{tot}}$, for different inclination angles α.

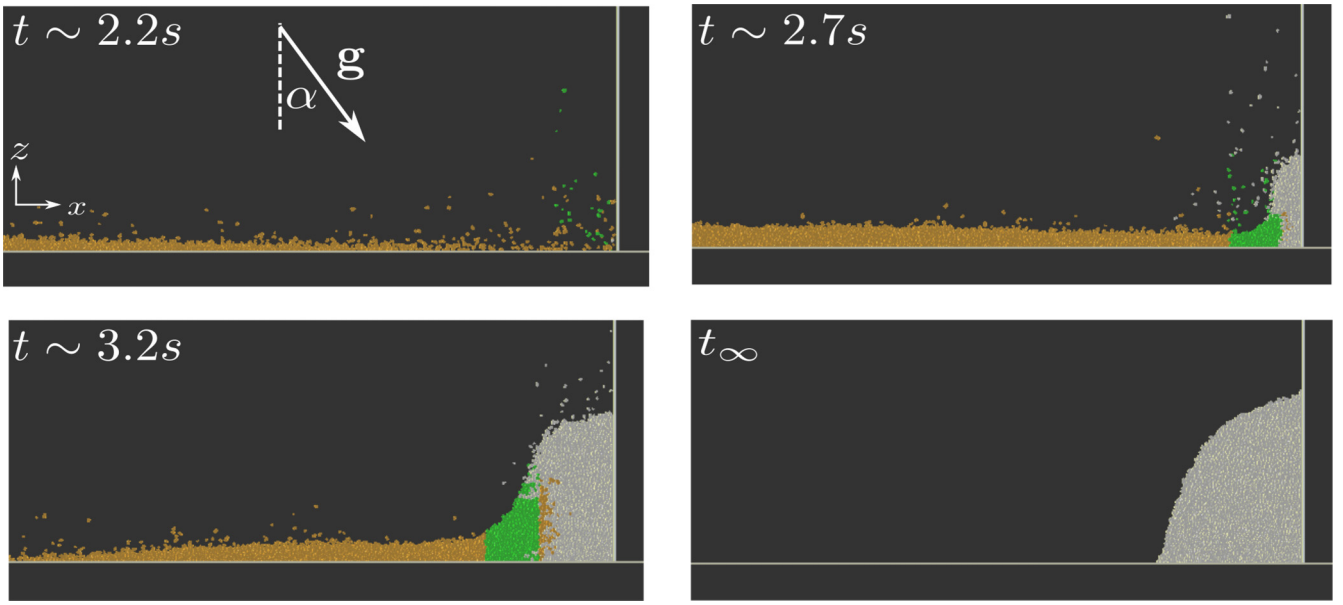

FIG. 4. DEM simulations. Snapshots taken at different times of the granular flow-wall interaction, as identified in Fig. 5. Example for $\alpha = 40^\circ$. Similar to Fig. 1, the region in brown corresponds to the undisturbed incoming flow, the region in white is the dead zone (see Sec. II B 3), and the region in green corresponds to the virtual box that roughly matches the jump length (as defined in Sec. II B 2).

mass is created. In contrast, this ratio goes up to 75% for $\alpha = 30^\circ$, where the impact force is dominated by the dead zone weight. These findings help in understanding qualitatively the proportion of the different contributions to the total force and their dependence on the incoming granular flow regime controlled by the slope (fast inertial regime at high α versus slow regime at lower α). Note that an eventual saturation of the force before the mass reaches its maximum value can be observed for $\alpha = 30^\circ$, in contrast to the case $\alpha = 35^\circ$ for which the peak is very small but still present.

Both Figs. 2 and 3 clearly show a change in behavior while moving from $\alpha = 35^\circ$ to $\alpha = 30^\circ$. This point will be further discussed.

2. *The different stages of the impact with the wall*

This section discusses the different stages of the impact with the rigid wall, as well as their relation with the volume fraction of both the granular incoming flow and the dead zone. For this aim, some details of an example of a simulation with inclination angle of 40° are presented. The normal impact force applied to the wall can be classified into different phases, as identified through the DEM snapshots provided in Fig. 4 backed by the signals given in Fig. 5.

First, the impact starts with a very dilute front impacting the rigid wall ($2.2 < t < 2.4$ s in Fig. 5; stage 1), driven by a very small value of ϕ_1 and no dead zone formation ($\phi_2 = 0$). The flow during this stage is too discrete (see top left snapshot of Fig. 4) and cannot be described by a continuum analytic model.

Afterwards, the second stage starts where the dilute front of the flow is strongly compressed due to the fast impact and a dead zone is created which has a volume fraction larger than that of the incoming flow. Next, both volume fractions get close to each other and keep increasing, which indicates the presence of the dense main body of the granular flow and also the fast-growing evolution of the dead zone ($2.6 < t < 2.9$ s in Fig. 5; stage 2). This is where a shock interface is identified and keeps growing upstream from the wall (see top right snapshot of Fig. 4). Still in this stage, the normal force keeps increasing almost linearly.

Then, for $t > 2.9$ s (see Fig. 5; stage 3), ϕ_1 value stabilizes for a short period as the main body of the flow continues to collide with the dead zone. Due to this collision, ϕ_2 keeps on increasing because of the compaction of the dead zone. These observations keep on going until reaching the peak force (at $t = 3.35$ s) at which ϕ_1 ends its stabilization period and ϕ_2 gets saturated. The bottom left panel of Fig. 4 corresponds to a snapshot before reaching the maximum in peak force.

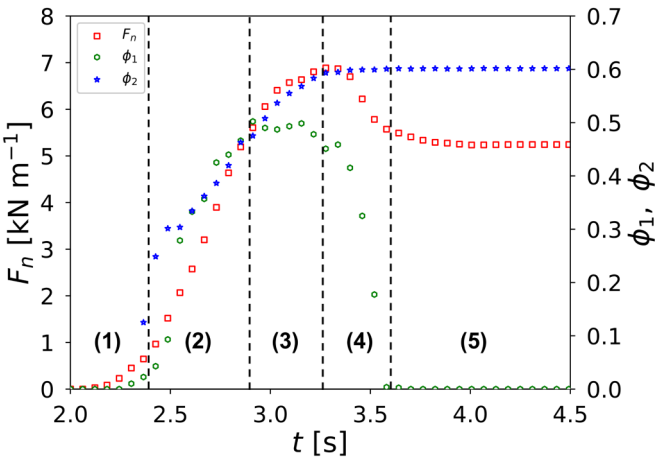

FIG. 5. DEM simulations. Evolution over time of the normal impact force F_n and volume fractions ϕ_1 and ϕ_2 of the granular flow and the dead zone, respectively. Identification of the different stages (from 1 to 5; see text for explanation) of the dry granular avalanche impact with the wall. Example for $\alpha = 40^\circ$.

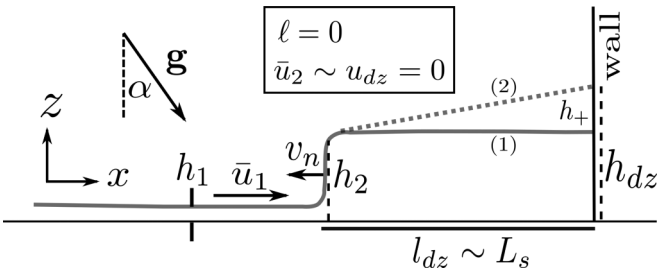

FIG. 6. Granular shock wave forming upstream of a wall of semi-infinite height, while grains are trapped between the wave and the wall: a simplified sketch with the main assumptions made for the analytic model. In particular, it is assumed that the length of the jump (defined in Fig. 1) tends toward zero: $\ell \to 0$. See text for notations.

The next stage is characterized by the reduction of the impact force as it goes to the residual one in a fast transition behavior (stage 4 in Fig. 5). Meanwhile, the volume fraction of the incoming flow decreases sharply as the tail of flow collides with the dead zone and ultimately vanishes.

Finally, the volume fraction inside the dead zone saturates to a value close to 0.6 and the force approaches the residual force against the wall that represents the apparent weight of the dead zone (stage 5 in Fig. 5). This corresponds to the snapshot shown in the bottom right panel of Fig. 4.

It can be concluded that the transient interaction between the granular flow and the rigid wall is complicated with different stages. In the following, we propose a depth-averaged continuum approach based on a compressible shock wave which coexists with a dead zone to capture the main underlying physics of that flow-wall interaction.

III. DEPTH-AVERAGED CONTINUUM APPROACH

A. Travelling shock wave and dead zone

This section describes the frontier between the incoming granular flow and the dead zone formed upstream of the wall by a hydrodynamiclike compressible wave, using a simple depth-averaged shock wave theory. Though the jump has a finite length ℓ (see Fig. 1), its volume is modeled as shrinking into a singular surface. This yields the simplified sketch of a shock wave depicted in Fig. 6, where $\ell = 0$.

A number of variables are defined on the sketch in Fig. 6. The filling height $h_{\rm dz}$ corresponds to the maximum height reached by the grains that pile-up against the wall, as already discussed in the previous section. Under the assumption $\ell = 0$, the length of the dead zone $l_{\rm dz}$ roughly matches the distance L_s between the wall and the shock wave (this point will be further discussed in the rest of the paper). The jump height h_2, the depth-averaged velocity $\bar{u}_2$, and the mean volume fraction ϕ_2 characterize the region downstream of the jump, on the rearward side of the shock. The propagation speed of the shock wave is v_n. The dead zone is characterized by a volume fraction $\phi_{\rm dz}$ close to static close packing ($\phi_{\rm dz} \approx 0.64$ in three dimensions [21]) and a mean velocity $u_{\rm dz} = 0$. The depth-averaged shock wave model proposed here is (by construction) unidirectional, meaning that the main velocity direction is along the slope. In practice, there exists a nonzero vertical (normal to the flow-bottom) component of velocity, as observed for instance in the discrete element simulations described in Sec. II. In the spirit of the shock wave model presented here, identifying the particles with zero velocity along the slope—whatever their velocity in the direction normal to the flow-bottom—is a more realistic definition of the dead zone to define the latter in the DEM simulations (see Sec. II B 3). Also, ϕ_2 is assumed to equal $\phi_{\rm dz}$. Under the assumption that $\ell = 0$, the variation of ϕ from ϕ_1 to ϕ_2 is not described. Instead, we consider a discontinuity in density, in addition to the discontinuity in height and velocity.

The integral forms, in their depth-averaged form, of mass and momentum conservation equations across the compressible shock wave traveling at speed v_n are (see more detail in [22] and a number of references therein):

$$[[\rho_P \phi h(\mathbf{u} - \mathbf{v_n}) \cdot \mathbf{n}]] w = 0, \tag{1}$$

$$\left[\left[\rho_P \phi h \mathbf{u}(\mathbf{u} - \mathbf{v_n}) \cdot \mathbf{n} + \tfrac{1}{2}\rho_P \phi g h^2 \cos\alpha \mathbf{n}\right]\right] w = \mathbf{S}. \tag{2}$$

The jump bracket $[[f]] = f_1 - f_2$ denotes the difference between the enclosed function f on the forward and rearward sides of the singular surface, following the notation commonly used in the literature about granular shocks described within the depth-averaged framework [23,24]. h and $\mathbf{u}$ denote the flow thickness and the mean velocity. The flow width is w and α is the slope angle, in accordance to notation already used for the DEM simulations. The product $\rho_P \phi$ is the density of the granular flow, where ρ_P holds for the intrinsic particle density. The term $\mathbf{S}$ denotes the source term associated with possible stresses acting within the finite jump volume.

The above shock equations are valid assuming a hydrostatic [$\sigma_{zz} = \rho g(h - z)\cos\alpha$] and isotropic ($k = 1$) distribution for pressure forces acting upon both sides of the jump, where $k = \sigma_{xx}/\sigma_{zz}$ denotes the ratio of normal stresses. Uniform velocity profiles are assumed too: $\beta = \overline{u^2}/\bar{u}^2 \sim 1$. Because the velocity profiles of incoming flows investigated in the present study typically show a slip velocity at the bottom, which is relatively large compared to the surface velocity (see Fig. 14 in Ref. [17]), this assumption for β is well founded. Detailed discussions on considering values of k and β slightly different from unity (either upstream or downstream of a shock) are provided in Refs. [22,25] and some other references therein. For a detailed investigation on the effect of k on the propagation of granular jumps upstream walls, we refer to the numerical work by Pudasaini and Kroner [3].

Note that a recent study on standing jumps formed in granular flows [22] has revealed the importance of the forces acting over the finite length of the jump—under certain circumstances—when the jumps become diffuse at low Froude numbers, the Froude number of the incoming flow being defined by $\mathrm{Fr}_1 = \bar{u}_1/\sqrt{g h_1 \cos\alpha}$. However, those forces are assumed here not to come into play, with respect to the assumption that the volume of the shock wave shrinks into a singular surface ($\ell = 0$ yields $\mathbf{S} = 0$ in the momentum equation). This important assumption will be discussed in more detail in Sec. V A when cross-comparing the analytic force model proposed here and the DEM simulations.

In the problem of granular impact against a wall of semi-infinite height, the normal velocity at the outgoing section of the jump has to satisfy the velocity continuity, thus leading

to $\bar{\mathbf{u}}_\mathbf{2} \cdot \mathbf{n} = u_{dz} = 0$. From mass conservation, this yields the following expression for the velocity v_n at which the granular shock propagates:

$$v_n = -\frac{(\bar{\mathbf{u}}_\mathbf{1} \cdot \mathbf{n})\mathbf{n}}{\frac{\phi_2}{\phi_1}\frac{h_2}{h_1} - 1}. \tag{3}$$

Note that it is generally observed that shallow granular flows down inclines are faster ($\bar{u}_1$ larger) and more dilute (ϕ_1 lower) and produce thicker jumps (h_2 higher; see, for instance, Ref. [22]), at high slope angles. Under the reasonable assumptions that h_1 (weakly sensitive to slope angle) and ϕ_2 (dense granular bulk at random close packing downstream of the jump) are nearly unchanged, Eq. (3) thus suggests that v_n will show little variation with slope because the increase of $\bar{u}_1$ with slope may counter-balance the increase of the product $\frac{\phi_2}{\phi_1}\frac{h_2}{h_1}$ with slope.

The jump height h_2 is by construction smaller or equal to h_{dz} (as drawn in Fig. 6) and can be predicted by injecting Eq. (3) for v_n in Eq. (2), which after some rearrangements takes the following form:

$$\left(\frac{h_2}{h_1}\right)^3 + A\left(\frac{h_2}{h_1}\right)^2 + B\left(\frac{h_2}{h_1}\right) + C = 0. \tag{4}$$

In the above form, we note $A = -1/\lambda_\phi$, $B = -(1 + 2Fr_1^2)/\lambda_\phi$ and $C = 1/\lambda_\phi^2$. The density ratio is $\lambda_\phi = \phi_2/\phi_1$. This equation is a cubic equation which can be solved by Cardano's method [26]. The thickness h_2 of the compressible jump, relative to the incoming flow thickness h_1, is then given by the physically meaningful (h_2/h_1 greater than 1) solution of Eq. (4) for $\Delta < 0$ (among the two other roots, one is negative and another one is smaller than 1):

$$\frac{h_2}{h_1} = 2r^{1/3}\cos\left(\frac{\theta_0}{3}\right) + \frac{1}{3\lambda_\phi}, \tag{5}$$

where r and θ_0 are defined as follows:

$$r = \frac{1}{2}\sqrt{q^2 - \Delta}, \tag{6}$$

$$\theta_0 = \arccos\left(-\frac{q}{2r}\right), \tag{7}$$

and $\Delta = q^2 + 4p^3/27$ and q and p are functions of Fr_1 and λ_ϕ:

$$q = \frac{1}{\lambda_\phi^2} - \frac{1}{27}\left(\frac{9\left(1 + 2\mathrm{Fr}_1^2\right)}{\lambda_\phi^2} + \frac{2}{\lambda_\phi^3}\right), \tag{8}$$

$$p = -\frac{1 + 2\mathrm{Fr}_1^2}{\lambda_\phi} - \frac{1}{3\lambda_\phi^2}. \tag{9}$$

Provided that the incoming flow conditions (h_1, $\bar{u}_1$, and ϕ_1) are known, the above description based on a simple depth-averaged compressible shock wave theory gives a prediction of h_2 and v_n. The latter parameters are the key ingredients needed to feed the analytic solution for the impact force on the rigid wall, as derived in the following section.

B. Impact force on the wall

Back to the simplified sketch given in Fig. 6, the impact force (normal to) on the rigid wall results from the apparent weight of the granular material squeezed between the incoming flow and the wall, plus a dynamic force caused by both the incoming flow and the shock. We now write the static equilibrium of the dead zone at a given time t, on the x-axis direction along the slope:

$$\Sigma F_{\mathrm{ext}} = F_s + W_{\mathrm{dz}}\sin\alpha - \mu_{\mathrm{dz}}W_{\mathrm{dz}}\cos\alpha + R = 0. \tag{10}$$

In the above equation, the components of the forces that come into play are defined: F_s is the force that the incoming flow exerts on the dead zone (mainly controlled by the interface described as a compressible shock wave), $W_{\mathrm{dz}}\sin\alpha$ is the weight of the dead zone, $\mu_{\mathrm{dz}}W_{\mathrm{dz}}\cos\alpha$ is the resistive friction force at the bottom where μ_{dz} is a Coulomb friction coefficient, and R is the reaction of the wall normal to the wall.

It follows therefore that the total normal force on the wall is given by

$$F_n = -R = F_s + W_{\mathrm{dz}}\cos\alpha(\tan\alpha - \mu_{\mathrm{dz}}). \tag{11}$$

The expressions for W_{dz} and F_s are given in the following sections. The value to be given to the Coulomb friction coefficient μ_{dz} will be discussed in more detail in Sec. V B.

1. Dead zone dynamics

One can get a rough approximation of the growth of the dead zone over time using the propagation speed of the shock wave. The distance L_s at which the shock is located at time $t + dt$ can be estimated from the value at time t using

$$\frac{dL_s}{dt} = v_n = \frac{\bar{u}_1}{\frac{\phi_2}{\phi_1}\frac{h_2}{h_1} - 1}. \tag{12}$$

In the above equation, v_n strictly corresponds to the theoretical value of the traveling speed of the shock wave, assuming $\ell = 0$. We do not account for any interaction—enduring frictional contacts, collisions—between the incoming grains (before the wave) and the grains that are trapped in the dead zone formed downstream of the wave. Moreover, the model is unidirectional, thus neglecting the vertical velocities. As such, v_n matches the speed at which the material is stored against the wall and: $l_{\mathrm{dz}} \simeq L_s$.

Because the shock wave continuum model assumes the shock to be a singular surface ($\ell = 0$, as shown in Fig. 6) rather than a volume, we stress here that the distance L_s derived from the model must be seen as only a rough estimation of l_{dz}. This point will be further discussed comparing the prediction of Eq. (12) to the dead zone length actually measured in the DEM simulations (see Sec. IV B 1).

Moreover, the jump height h_2 (height of the shock interface) is not always exactly equal to the filling height h_{dz} against the wall. The height h_2 is expected to be lower than h_{dz} depending on the dead zone shape: see case (2) in Fig. 6, where an extra term h_+ must be considered in the total run-up. The latter situation is in contrast with the case (1) sketched on Fig. 6, which corresponds to a dead zone that is nearly rectangular. This case (1) may happen if the slope α is lower than a typical macroscopic friction angle φ_M associated with quasistatic deformations, as shown on Fig. 1. The case (2) holds for a dead zone having constant slope and may occur when the slope α is greater than φ_M, as shown on Fig. 4. In this

case, the slope of the deposit (made with horizontal) is nearly equal to φ_M.

The weight of the dead zone is given by the following relation:

$$W_{\rm dz} = \rho_P \phi_{\rm dz} g c_{\rm dz} l_{\rm dz} \left(\frac{h_{\rm dz} + h_2}{2} \right) w, \tag{13}$$

where c_{dz} holds for a shape coefficient: $c_{\rm dz} > 1$ if $h_+ = h_{\rm dz} - h_2$ is nonzero ($\alpha \geqslant \varphi_M$), while $c_{\rm dz} = 1$ if $h_{\rm dz} = h_2$ ($\alpha \leqslant \varphi_M$). Those two distinct cases were identified in past laboratory tests [2,3,27] and analyzed with the help of numerical simulations based on depth-averaged shallow-water theory applied to granular flows [3].

If it is assumed that the slope of the dead zone free-surface made with the horizontal is constant over time and equal to the macroscopic friction angle φ_M associated with quasi-static deformations (for $\alpha \geqslant \varphi_M$; $h_+ = 0$, otherwise):

$$\tan(\alpha - \varphi_M) = \frac{h_+}{l_{\rm dz}}, \tag{14}$$

$h_{\rm dz}$ then takes the following form:

$$h_{\rm dz}(t + dt) = \max[h_2(t + dt), h_{\rm dz}(t)] + l_{\rm dz} \tan(\alpha - \varphi_M), \tag{15}$$

Note that in the relations above, the maximum between $h_2(t + dt)$ and $h_{\rm dz}(t)$ has been considered. This step is needed to avoid the (unphysical) decrease of the filling height $h_{\rm dz}$, while the jump height h_2 starts vanishing (as a result of the fact that the incoming flow starts dying). And the value of $h_{\rm dz}$ at time $t + dt$ can be estimated from the value at time t using:

$$\frac{dh_{\rm dz}}{dt} = \frac{dh_2}{dt} + \tan(\alpha - \varphi_M) \frac{dl_{\rm dz}}{dt} \simeq \frac{dh_2}{dt} + v_n \tan(\alpha - \varphi_M). \tag{16}$$

2. Force of the incoming flow

The normal force (along the slope) of the incoming flow exerted on the dead zone can be predicted by using the integral form of the momentum conservation across the shock formed between the incoming flow and the dead zone (using again the notation $[[f]] = f_1 - f_2$):

$$\left[[[\rho_P \phi h \mathbf{u}(\mathbf{u} - \mathbf{v_n}) \cdot \mathbf{n}]] - \left[\left[\int_0^h \sigma_{xx} dx \right] \right] \mathbf{n} \right] w = 0. \tag{17}$$

The source terms associated with what could happen over the finite length ℓ of the jump are still neglected here. Hydrostatic isotropic pressure distribution is assumed for the incoming granular flow (section defined by $h = h_1$, just before the shock):

$$\int_0^{h_1} \sigma_{xx_1} dx = \frac{1}{2} \rho_P \phi_1 g h_1^2 \cos\alpha. \tag{18}$$

The force $F_s = -w \int_0^{h_2} \sigma_{xx_2} dx$ (section defined by $h = h_2$, just after the shock) of the incoming flow on the dead zone is then given by the relation:

$$F_s = \rho_P \phi_1 h_1 \bar{u}_1^2 \left(1 + \frac{\phi_1 h_1}{[[\phi h]]} \right) w + \frac{1}{2} \rho_P \phi_1 g h_1^2 w \cos\alpha, \tag{19}$$

which can be rearranged in the following form:

$$F_s = \rho_P \phi_1 \bar{u}_1^2 h_1 w \left(1 + \frac{1}{\frac{\phi_2}{\phi_1}\frac{h_2}{h_1} - 1} + \frac{1}{2{\rm Fr}_1^2} \right). \tag{20}$$

3. Total force on the wall

Equation (11) fed with the expressions for W_{dz} [Eq. (13)] and F_s [Eq. (20)] gives the total force on the wall. If one considers the inertial ($\propto \rho_P \phi_1 \bar{u}_1^2 h_1 w$) and depth-dependent ($\propto \rho_P \phi_1 g h_1^2 w$) forces associated with the depth-averaged features $\bar{u}_1$, h_1, and ϕ_1 of the incoming flow, the total force on the wall can take the following form:

$$F_n = \tfrac{1}{2} \mathcal{C} \rho_P \phi_1 \bar{u}_1^2 h_1 w + \tfrac{1}{2} \mathcal{K} \rho_P \phi_1 g h_1^2 w \cos\alpha, \tag{21}$$

where the prefactors $\mathcal{C}$ and $\mathcal{K}$ are time-dependent parameters given by the following relations:

$$\mathcal{C} = 2 \left(1 + \frac{1}{\lambda_\phi \frac{h_2}{h_1} - 1} + \frac{1}{2{\rm Fr}_1^2} \right), \tag{22}$$

$$\mathcal{K} = c_{\rm dz} (\tan\alpha - \mu_{\rm dz}) \lambda_\phi \frac{l_{\rm dz} h_{\rm dz}}{h_1^2}, \tag{23}$$

where $\ell_{\rm dz}$ can be derived from Eq. (12).

IV. SHOCK WAVE MODEL VERSUS DEM SIMULATIONS

The comparison between the DEM results (Sec. II) and the shock wave continuum approach proposed (Sec. III) is based on the evolution over time of (i) the impact force, (ii) the height of the jump, and (iii) the length of the dead zone upstream from the wall. This comparison is done over the entire range of slope inclinations investigated by the DEM simulations. Unless specified otherwise, the analytical calculation is implemented by feeding the model with the depth-averaged variables h_1, $\bar{u}_1$, and ϕ_1 averaged over the length of the virtual box taken equal to $15 d_{50}$, and a set of fixed parameters: $\phi_2 = 0.6$ (typical volume fraction of the dead zone), $c_{\rm dz} = 1$, $\mu_{\rm dz} = 0$, and $\varphi_M = 31^\circ$. The values chosen for the last three parameters will be further discussed in the following.

A. Normal force applied to the wall

Figure 7 shows the results from DEM simulations compared with the force model from shock theory in terms of the normal force applied by the flow to the rigid wall.

For all slopes, at the very beginning of the impact, the model does not predict the impact force because, for this stage, the flow front impacting the wall is too dilute (granular gas) to be described by the continuum model proposed. The latter is built on the assumption of a dead zone downstream of the shock which is denser than the incoming flow. This assumption is not valid when the dilute granular front starts impacting the wall: the volume fraction of the dilute front—namely the assembly of grains located between the wall and the incoming flow, is much lower than the volume fraction of the main body of the incoming, much denser, flow.

Afterwards, for all α, the model predicts qualitatively well the evolution of impact force with time, in comparison with DEM. Moreover, the transition from the peak to residual force is generally well predicted except for $\alpha = 30^\circ$ for which the

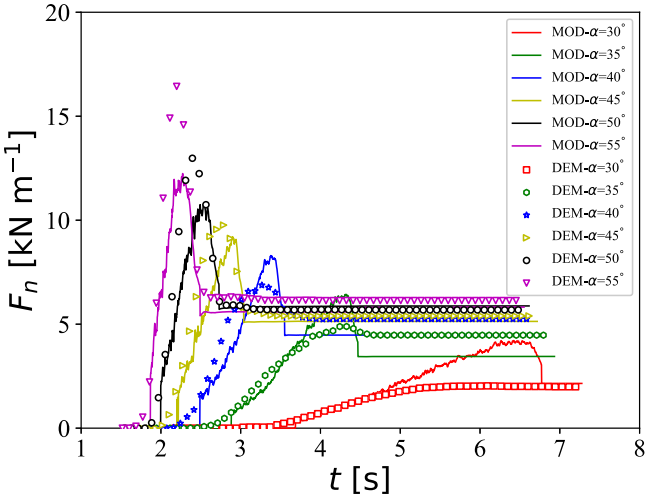

FIG. 7. Evolution of the normal impact force F_n with time, for different inclination angles: cross-comparison between the DEM simulations and the analytic force model based on shock wave continuum approach (with $\phi_2 = 0.6$, $c_{\mathrm{dz}} = 1$, $\mu_{\mathrm{dz}} = 0$, and $\varphi_M = 31°$).

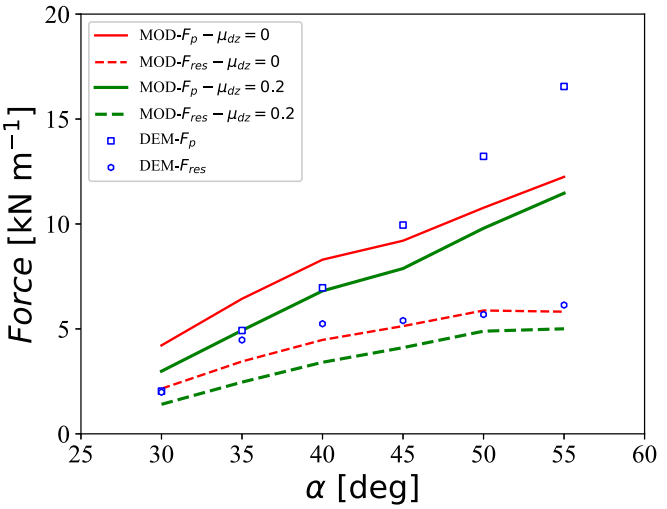

FIG. 8. Peak and residual forces—extracted from the typical time-series shown in Fig. 7—versus the slope angle α: comparison between the analytic force model (solid and dashed lines for the peak and residual forces, respectively) and DEM simulations (dots). Two predictions of the analytic force model are shown for $\mu_{\mathrm{dz}} = 0$ (red lines) and $\mu_{\mathrm{dz}} = 0.2$ (green lines).

model predicts a big peak, which is not observed in DEM. For intermediate values of α (40–45°), the peak force is quite well captured by the shock model. For the highest α, the model underestimates the peak force (this point will be further discussed in Sec. V A), whilst it overestimates the peak force for lower α. For the lowest α (30–35°), much less agreement is observed as the model tends to overestimate the maximum impact force. This result could be because as the slope angle decreases, the shock tends to be more diffuse. As such, the analytic model based on shock theory with $\ell = 0$ (sketch of Fig. 6) becomes much less relevant. Processes that dissipate energy over the finite length of the jump should be considered. The changes in the shape of the dead zone (variation of c_{dz} over time) might also be a source of divergence between the analytic force model and DEM, as well as the fact that the basal friction, μ_{dz}, was taken equal to zero in the analytic force model. The latter point is further analysed thereafter.

Figure 8 shows the peak and residual force values for both the analytic force model and DEM for the full range of investigated slopes. For the peak force, the model agrees well with DEM simulations at intermediate values of α (40–45°). The peak force is largely underestimated for higher α ($\geqslant$50°) and overestimated for smaller α ($\leqslant$35°). A discussion on these differences and their relation with the slope angle and parameters sampling will be detailed in Sec. V A. For the residual force, the increase with slope angle is well reproduced by the model over the full range of slope angles tested, as shown in Fig. 8.

Note that choosing a non zero basal friction ($\mu_{\mathrm{dz}} = 0.2$ for instance) instead of $\mu_{\mathrm{dz}} = 0$ yields better results for the peak force at the lowest α but is worse for the residual force for all α, as shown by the green lines in Fig. 8. In Sec. V B, we point out how the processes involved in the friction with the bottom are complicated, by showing how the mean value of τ_{xy}/σ_{zz} at the base measured in DEM varies with time for the lowest α.

B. Shock wave and dead zone dynamics

1. Distance the shock interface travels upstream

In this section, the distance—along the chute bottom—between the shock interface and the wall is compared between the shock theory and the DEM simulations. The model predicts a distance L_s, which locates the position of the traveling shock wave. Since a singular surface is assumed, this length is thought to be similar to the length of the dead zone l_{dz} (see sketch drawn in Fig. 6). From DEM, we could quantify with precision the length l_{dz} of the dead zone, as detailed in Sec. II B 3. Figure 9 shows the evolution with time of both L_s estimated from the model and l_{dz} actually measured in DEM.

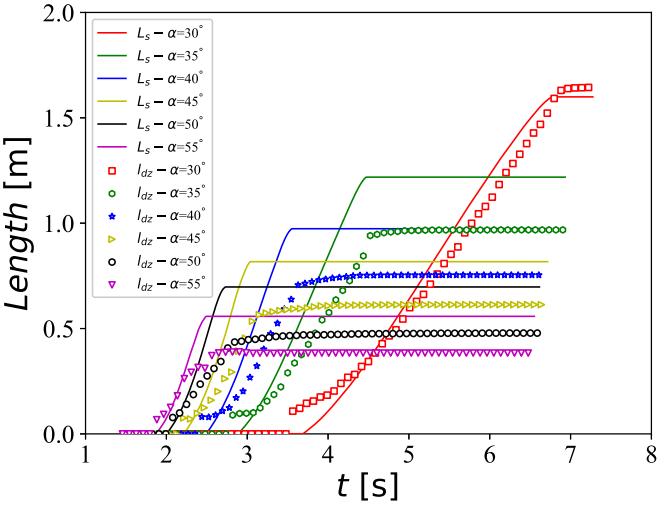

FIG. 9. Evolution over time of the dead zone length l_{dz} measured from DEM (dots) and of the distance L_s between the wall and the shock interface, estimated from the analytic model (solid lines). The comparison is shown for different slope angles.

Before the saturation of L_s, the distance from the propagating shock to the wall is generally higher than that of the dead zone. This is consistent with the assumption of a singular surface for the shock theory ($L_s = l_{\rm dz} + \ell$ being greater than $l_{\rm dz}$). A good agreement between the model and DEM is generally observed regarding the evolution over time, but the final value is not captured. The gap between L_s, predicted by the shock model, and $l_{\rm dz}$, measured in DEM, is explained by the fact that some important yet complex aspects of the physics of the flow-wall interaction are not accounted for. In practice, it is mostly likely that the traveling speed is actually smaller than the theoretical value of v_n given by Eq. (3) because of some dissipation processes (enduring frictional contacts, collisions) at stake over the finite length of the jump. Moreover, for high slope angles, a significant part of the incoming flow gets diverted in the y direction and thus is not accounted for in the unidirectional model under consideration. As a result, the value of L_s, predicted from the shock theory, should then be always considered as an overestimation of $l_{\rm dz}$, which is indeed observed for all slope angles except for $\alpha = 30^\circ$ for which L_s and $l_{\rm dz}$ are similar.

2. *Jump height and run-up against the wall*

Figure 10 shows the evolution over time of the run-up $h_{\rm dz}$ measured in DEM (dots) compared to the sum of the jump height h_2 predicted by shock theory and the extra run-up h_+ using Eq. (15) (solid lines) for different slope angles.

The shock model is not able to capture the early stage of the increase of $h_{\rm dz}$ with time measured in DEM and generally overestimates it. After this early stage for which the shock model is poor, it is interesting to observe that the evolution over time is better captured, especially for the high slope angles ($\alpha = 40^\circ$–55°). This is the proof that the contribution caused by the additional run-up h_+ (see in Fig. 11 an example of that situation) is quite well described with the set of Eqs. (14)–(16).

For α lower than 40°, the final run-up is very well captured. Those tests correspond to tests for which the dead zone close to the wall is flat (parallel to the flow-bottom) and the jump is more diffuse, as illustrated by the snapshot extracted from

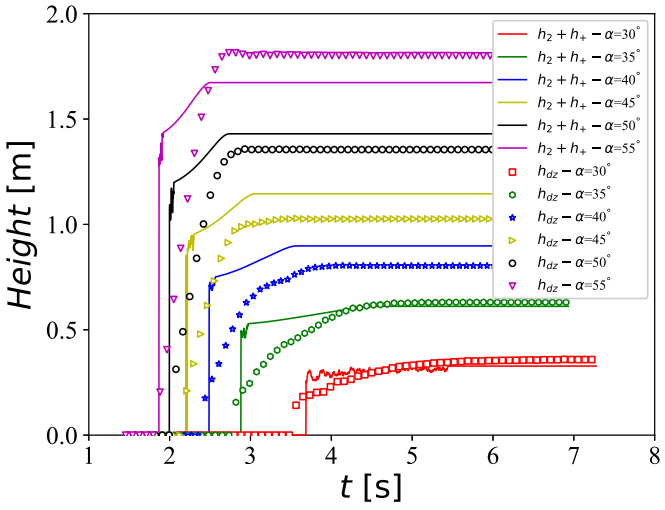

FIG. 10. Evolution with time of the filling height $h_{\rm dz}$ measured from DEM (dots) and of the sum of jump height h_2 predicted by shock theory and extra run-up h_+ (solid lines).

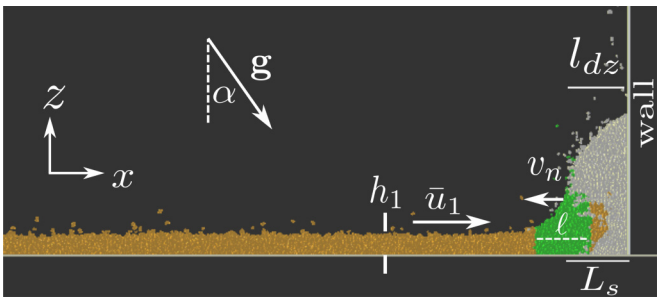

FIG. 11. DEM simulations: snapshot of a simulation performed at $\alpha = 40^\circ$. The free-surface of the dead zone (white region), close to the wall, is not parallel to the flow-bottom: $h_{\rm dz} - h_2 = h_+ > 0$.

a DEM simulation at $\alpha = 30^\circ$ in Fig. 1. For the highest $\alpha = 55^\circ$, the final value is underestimated by the model, while it is overestimated for intermediate slope angles ($\alpha = 40^\circ$–50°). The result that $h_2 + h_+$ predicted by the model is lower than h_{dz} measured in DEM at the highest α may be attributed here to the fact that the movement in y direction is not accounted for in the shock model proposed.

V. DISCUSSION AND CONCLUSION

A. Length over which h_1, $\bar{u}_1$, and ϕ_1 are averaged

The predictions from the shock theory discussed until now were obtained by feeding the set of equations presented in Sec. III with the incoming flow conditions averaged over a constant distance $15d_{50}$. Five other lengths ($5d_{50}$, $10d_{50}$, $20d_{50}$, $25d_{50}$, and $35d_{50}$) were tested to further analyze the influence of this crucial parameter on the results. The sensitivity of peak and residual forces—as functions of the slope angle—to these different input flow conditions is shown in Fig. 12.

The results in terms of peak force show that choosing a short sampling length ($5d_{50}$ or $10d_{50}$) gives very poor results. The peak force is not—or very weakly—sensitive to increasing the sampling length from $15d_{50}$ to $35d_{50}$ at low slope angles. In contrast, it becomes more sensitive to the sampling length for higher α ($\alpha > 42^\circ$) and the results are nearly perfect for the sampling length equal to $35d_{50}$. The kinetic contribution, mainly driven by the velocity $\bar{u}_1$, to the total force is dominant at high slope angles and is strongly influenced by the sampling length. DEM simulations showed that internal disturbances (changes in velocity profiles) propagate far upstream in the incoming flow, well beyond the location where the free surface would suggest the beginning of the jump. This physics at high slope angles will need further investigation in the future. By considering a larger sampling length, we avoid $\bar{u}_1$ to be damped and $F_{\rm peak}$ to be underestimated, as it is for intermediate sampling lengths between $15d_{50}$ and $25d_{50}$. At lower slope angles, the peak force (not sensitive to the sampling length in the $15d_{50}$ to $35d_{50}$ range) is always overestimated. Preliminary analysis (graphs not shown here) show that the dead zone surface is not sensitive to the sampling length, though both the filling height and the length of the dead zone are. This shows that the dead zone dynamics can be quite well predicted but the force model is not suitable, thus suggesting we are missing some physics at low slope angles. In short, the singular shock model is not able to transform properly the kinetic force of the incoming flow into the force caused by the apparent weight of

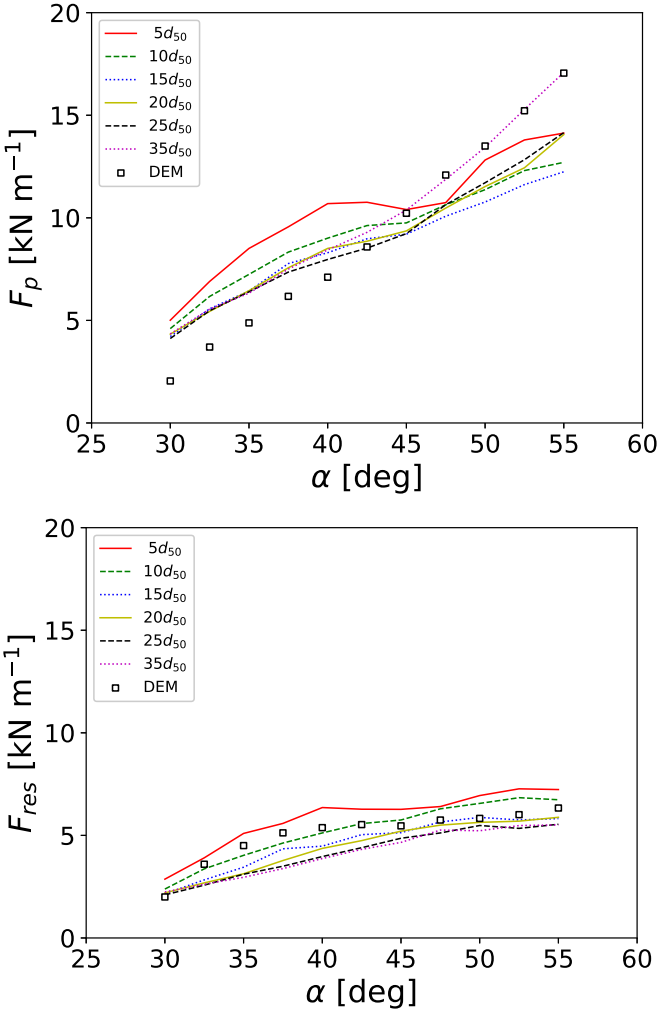

FIG. 12. Peak force (top) and residual force (bottom) versus α: comparison between DEM (dots) and the shock theory for six different lengths over which the input conditions for the incoming flows are averaged.

the dead zone, which is dominant at low slope angles. This is clear from Fig. 7, where the peak force produced by the model is generally more pronounced than the one measured in DEM at low α. The results in terms of residual force show that the sensitivity to the sampling length does exist but is much less pronounced than for the peak force.

A key result is that we can reproduce fairly well the dead zone dynamics and the time-histories of impact force for a wide range of slope's inclinations, provided that the analytic force model is fed with the incoming flow conditions averaged over a certain length. However, the sensitivity (which is significant for the peak force) of the results to that sampling length brings us back to the crucial assumption initially made to derive the analytic force model. We assumed a compressible shock wave that shrinks into a singular surface, thus implying $\ell \to 0$ and $\mathbf{S} = 0$ in Eq. (2). This assumption will deserve further work in the future, as it will be discussed in Sec. V C.

B. Friction at the base of the dead zone

Another point will need further analysis in the future. It is worthwhile to remind here that the analytic force model was computed considering either $\mu_{\mathrm{dz}} = 0$ for model calculations or a constant value arbitrarily equal to 0.2 (see Fig. 8).

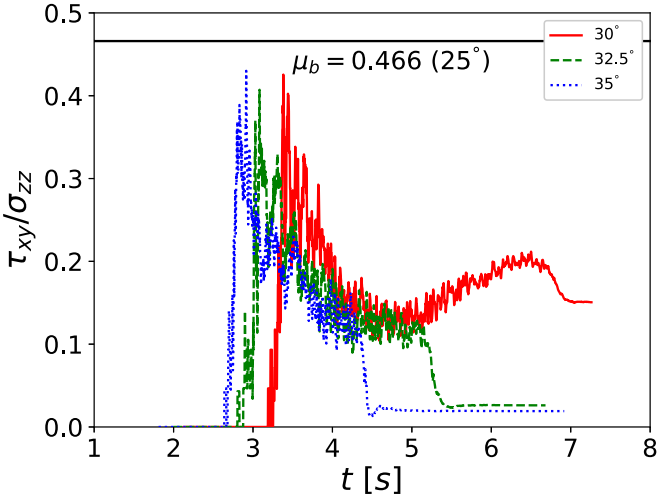

FIG. 13. Evolution with time of the ratio τ_{xy}/σ_{zz} measured in DEM for $\alpha = 30°$, 32.5°, and 35°. The horizontal line shows the microscopic friction μ_b, used in DEM, between the flow-bottom and each grain in contact with the flow-bottom.

The link between the μ_{dz} effective friction defined in the frame of the depth-averaged shock model and the friction at the base measured in DEM simulations remains unclear. However, it is interesting to check what happens at the base of the dead zone formed upstream of the wall. Figure 13 shows the evolution over time of the mean of τ_{xy}/σ_{zz} measured in DEM for the lowest slope angles tested. This graph does put emphasis on how the physics is complicated, through showing the highly transient evolution of τ_{xy}/σ_{zz} during the course of the flow-wall interaction. The ratio τ_{xy}/σ_{zz} is consistently always lower than the microscopic friction μ_b used in DEM between the flow-bottom and each grain in contact with the flow-bottom (see horizontal line in Fig. 13). It rises rapidly (first stage of impact with the wall), peaks, and then decreases before reaching a nearly constant but weak value around 0.13. The latter value does not depend too much on α. Finally, it drops (over a very short time) to a very small value when the avalanche comes to standstill. The latter behavior is not observed for the lowest $\alpha = 30°$ but an increase of τ_{xy}/σ_{zz} is observed instead. Implementing such a complicated physics in the depth-averaged shock model proposed remains a challenging question.

C. Concluding remarks

The present paper described the derivation of an analytic model to predict the impact of a granular avalanche flow on a rigid wall of semi-infinite height (overflow prevented). This analytic model is based on depth-averaged equations for a compressible shock wave traveling upstream of the wall, while a dead zone forms between the shock and the wall. It allows the estimation of the time evolution of the dead zone length, the run-up against the wall and the total force on the wall.

The model was able to capture fairly well the dead zone dynamics and the impact force over time measured with the

help of simulations of the flow-wall impact problem based on discrete element simulations. Such a result was made possible by feeding the analytical force model with the input flow conditions h_1, $\bar{u}_1$, and ϕ_1 (obtained from DEM) averaged over a constant length $15d_{50}$ (green region upstream of the dead zone shown on the snapshots in Figs. 1, 4, and 11) and minimal assumptions for the friction mobilized at the base of the dead zone (see Sec. V B). Feeding the analytic force model with the flow conditions measured in DEM at a singular surface—either at a section of the undisturbed flow just before the beginning of the shock or at a section just before the dead zone—did not work. Increasing the length of averaging for h_1, $\bar{u}_1$, and ϕ_1 did not work either, except for the highest slope angles where very good results were obtained in terms of peak force.

Our study revealed that choosing a length scale over which we averaged the incoming flow condition equal to $15d_{50}$ could be a conservative choice to obtain good results for the wide range of slope angles tested not only in terms of impact force time evolution but also in terms of dead zone dynamics (length and run-up against the wall). Given the simple assumptions made (singular shock), this success should be stressed. However, some issues were identified concerning both the peak force and the residual force. On one side, the peak force was much better captured at high slope angles by increasing the sampling length from $15d_{50}$ to $35d_{50}$. We detected internal disturbances propagating far upstream and thus damping the incoming flow. This led to a significant sensitivity of the model prediction in terms of peak force to the sampling length. In particular, velocity and peak force (controlled by velocity) were largely underestimated at high slope angles ($>42.5^\circ$) when using a sampling length smaller than $35d_{50}$. This question will need further investigation in the future. On the other side, the dead zone dynamics and the residual force were weakly sensitive to the sampling length whatever the slope angle. The residual force was systematically underestimated for the low slope angles ($<42.5^\circ$), except for the lowest slope angle (30°). This shows that some physics is still missing: the complicated dynamics of the diffuse jump co-existing with the dead zone is not fully captured by the shock wave model, though the time-histories of both the dead zone length and the run-up against the wall measured in DEM were relatively well reproduced.

The need of averaging the incoming flow conditions over a constant length to get reasonable results is interpreted as a mean to offset the assumption that the shock wave shrinks into a singular surface. This point will deserve much more attention in the future. Work is now under progress to develop new depth-averaged solutions for traveling shock waves, accounting for the finite length of those waves in the wake of the recent study proposed by Ref. [28] for standing jumps. This will offer an additional degree of freedom in the jump equation that may help to improve the results regarding the force time history. However, the new solutions will need a prediction for the finite length of the jump, in addition to a relevant constitutive law for the friction force acting over the jump length, as already pointed out in the case of standing jumps formed in flows of granular materials down inclines [22,28]. Dry granular materials are highly dissipative and thus able to dissipate a lot of energy over a short length, in strong contrast to water. More detailed studies are needed to crucially decipher what happens in the interior of the jumps to be able to develop new models for the prediction of the jump geometry and their propagation when a flow impacts a wall and those jumps coexist with a dead zone.

ACKNOWLEDGMENTS

Thierry Faug is grateful for financial support from the People Programme (Marie Curie Actions) of the European Union's Seventh Framework Programme under REA Grant Agreement No. 622899 (FP7-PEOPLE-2013-IOF, GRAIN-PACT). The authors thank two anonymous referees for their insightful comments and suggestions on this study.

APPENDIX A: DISCRETE ELEMENT METHOD (DEM)

The numerical simulations of the dry granular flow impact on the rigid wall were carried out using DEM. Nowadays DEM is widely used for modeling granular media. It is particularly efficient for both static and dynamic simulations of granular assemblies where the medium can be described at a microscopic scale. The method is based on an explicit numerical integration proposed by Cundall and Strack [16]. It applies for collection of discrete bodies interacting with each other by a contact law. Different contact forces can be considered in different directions; the normal direction and also the tangential direction. Calculations alternate between the application of Newton's second law to particles' motion, and of a force-displacement law resulting from the interaction models.

YADE software was used as a modeling tool, which is an extensible open-source framework for discrete numerical models, focused on DEM [29].

A linear spring-dashpot contact law with a Mohr-Coulomb failure criterion was adopted where normal and tangential contact forces $\boldsymbol{F_n}$ and $\boldsymbol{F_t}$ between interacting bodies were calculated as follows:

$$\boldsymbol{F_n} = (k_n u_n - \gamma_n \dot{u}_n)\boldsymbol{n} \tag{A1}$$

$$\boldsymbol{F_t} = \begin{cases} \frac{k_t \boldsymbol{u_t}}{|k_t \boldsymbol{u_t}|} |\boldsymbol{F_n}| \tan\Phi & \text{if } |k_t \boldsymbol{u_t}| > |\boldsymbol{F_n}| \tan\Phi \\ k_t \boldsymbol{u_t} & \text{otherwise,} \end{cases} \tag{A2}$$

where k_n and k_t are the normal and tangential stiffness parameters, u_n and u_t are the normal and shear displacements, Φ is the interparticle friction angle, and γ_n is the normal viscous damping coefficient.

The normal stiffness of the contact between two particles (k_n) was calculated as [30]

$$k_n = \frac{2E_1 r_1 E_2 r_2}{E_1 r_1 + E_2 r_2}, \tag{A3}$$

where E_1 and E_2 are the elastic moduli of the first and second particles, respectively (both taken as 10^8 Pa), and r_1 and r_2 are the radii of the first and second particles, respectively.

The shear stiffness of the contact (k_t) was taken as $\frac{2}{7}k_n$ according to what was previously suggested by Silbert *et al.* [31]. Based on Schwager and Pöschel [32], with the restitution coefficient ε being the ratio between velocities after and before the impact, $\varepsilon_{n,t}$ and $\beta_{n,t}$ (normal and tangential restitution

coefficient) can be calculated as follows:

$$\varepsilon_{n,t} = \frac{\dot{u}(t_c^0)}{\dot{u}(0)} = e^{-\beta_{n,t}\pi/\omega_{n,t}} \tag{A4}$$

and

$$\beta_{n,t} = \frac{\gamma_{n,t}}{m_{\text{eff}}}, \tag{A5}$$

with

$$\omega_{n,t} = \sqrt{\left(\frac{2k_{n,t}}{m_{\text{eff}}}\right)^2 - \beta_{n,t}^2}. \tag{A6}$$

In the above relations, t_c is the duration of collision, $m_{\text{eff}} = (1/m_1 + 1/m_2)^{-1}$ is the effective mass, where m_1 and m_2 are the masses of two interacting particles, and $\dot{u}(t_c^0)$ and $\dot{u}(0)$ are velocities after and before the collision, respectively. The time step Δt was set to a value lower than the critical time step Δt_c to guarantee the stability of the numerical scheme [29].

APPENDIX B: DEM MODEL VALIDATION ON LABORATORY TESTS

Simulations using the same DEM model [15,17] were previously compared with existing small-scale laboratory data of a granular flow composed of gravel particles prepared with different samples' sizes and inclination angles [10]. This experimental data set was selected because it considered coarse-grained flows made of real gravel particles. In addition, the study provided detailed measurements of normal impact force applied to different heights (different segments of the rigid wall). The calibration was based on flow thickness measurement and final shape of the deposit behind the wall. A value of 0.3 for the coefficient of restitution was found to be suitable to reproduce the measurements made on the laboratory granular flows. In addition, using nonspherical particles in DEM was found to get better representation of the final deposit shape behind the wall [15]. Each DEM particle was initially created as a spherical particle with radius R and then replaced with an equivalent volume of two identical spheres with a radius R' overlapping over a distance R', where $R = \sqrt[3]{\frac{16}{27}}R'$. Clumps were treated as rigid bodies. The validation of the DEM model with the experimental data was based on the normal impact force and bending moment applied to the wall. The DEM model and experimental data were found to agree in terms of the value of the maximum impact force and maximum bending moment, time at which the maximum takes place, and also the final residual value of the force and bending moment [17].

[1] M. C. Chiou, Y. Wang, and K. Hutter, Acta Mech. **175**, 105 (2005).
[2] S. Pudasaini, K. Hutter, S. Hsiau, S. Tai, Y. Wang, and R. Katzenbach, Phys. Fluids **19**, 053302 (2007).
[3] S. P. Pudasaini and C. Kroner, Phys. Rev. E **78**, 041308 (2008).
[4] R. Valentino, G. Barla, and L. Montrasio, Rock Mech. Rock Eng. **41**, 153 (2008).
[5] S. Moriguchi, R. I. Borja, A. Yashima, and K. Sawada, Acta Geotechnica **4**, 57 (2009).
[6] H. Teufelsbauer, Y. Wang, M. C. Chiou, and W. Wu, Granular Matter **11**, 209 (2009).
[7] D. Mancarella and O. Hungr, Can. Geotech. J. **47**, 827 (2010).
[8] S. H. Chou, L. S. Lu, and S. S. Hsiau, Granular Matter **14**, 719 (2012).
[9] X. Cui and J. Gray, J. Fluid Mech. **720**, 314 (2013).
[10] Y. J. Jiang and I. Towhata, Rock Mech. Rock Eng. **46**, 713 (2013).
[11] C. Y. Kuo, L. T. Sheng, S. Y. Chiu, Y. Z. Yang, Y. C. Tai, and S. S. Hsiau, Phys. Fluids **27**, 013305 (2015).
[12] T. Faug, Phys. Rev. E **92**, 062310 (2015).
[13] H. Teufelsbauer, Y. Wang, S. P. Pudasaini, R. I. Borja, and W. Wu, Acta Geotechnica **6**, 119 (2011).
[14] J. M. N. T. Gray, Y. C. Tai, and S. Noelle, J. Fluid Mech. **491**, 161 (2003).
[15] A. Albaba, S. Lambert, F. Nicot, and B. Chareyre, Granular Matter **17**, 603 (2015).
[16] P. A. Cundall and O. D. Strack, Geotechnique **29**, 47 (1979).
[17] A. Albaba, S. Lambert, F. Nicot, B. Chareyre, in *Recent Advances in Modeling Landslides and Debris Flows* (Springer, Berlin, 2015), pp. 95–105
[18] T. Faug, R. Beguin, and B. Chanut, Phys. Rev. E **80**, 021305 (2009).
[19] B. Chanut, T. Faug, and M. Naaim, Phys. Rev. E **82**, 041302 (2010).
[20] T. Faug, P. Caccamo, and B. Chanut, Phys. Rev. E **84**, 051301 (2011).
[21] D. Cumberland and R. Crawford, *The Packing of Particles*, Vol. 6 of Handbook 212 of Powder Technology (Elsevier, Amsterdam, 1987).
[22] T. Faug, P. Childs, E. Wyburn, and I. Einav, Phys. Fluids **27**, 073304 (2015).
[23] K. M. Hákonardóttir and A. J. Hogg, Phys. Fluids **17**, 077101 (2005).
[24] J. M. N. T. Gray and X. Cui, J. Fluid Mech. **579**, 113 (2007).
[25] T. Faug, AIP Conf. Proc. **1542**, 642 (2013).
[26] G. Cardano and C. Spon, Opera Omnia **4**, 221 (1968).
[27] K. M. Hákonardóttir, *The Interaction between Snow Avalanches and Dams*, Ph.D. thesis, School of Mathematics, University of Bristol 2004.
[28] S. Mejean, T. Faug, and I. Einav, J. Fluid Mech. **816**, 331 (2017).
[29] V. Šmilauer, E. Catalano, B. Chareyre, S. Dorofeenko, J. Duriez, A. Gladky, J. Kozicki, C. Modenese, L. Scholtès, L. Sibille, J. Stránsk, and K. Thoeni, *Yade Documentation* (2010), retrieved from http://yade-dem.org/doc/.
[30] E. Catalano, B. Chareyre, and E. Barthélémy, Int. J. Numer. Anal. Methods Geomech. **38**, 51 (2014).
[31] L. E. Silbert, D. Ertaş, G. S. Grest, T. C. Halsey, D. Levine, and S. J. Plimpton, Phys. Rev. E **64**, 051302 (2001).
[32] T. Schwager and T. Pöschel, Granular Matter **9**, 465 (2007).